Design and performance of the collective Thomson scattering receiver at ASDEX Upgrade.

Furtula, Vedran; Salewski, Mirko; Leipold, Frank; Michelsen, Poul; Korsholm, Søren Bang; Meo, Fernando; Moseev, Dmitry; Nielsen, Stefan Kragh; Pedersen, Morten Stejner; Johansen, Tom Keinicke

Published in:
Review of Scientific Instruments

Link to article, DOI:
10.1063/1.3675886

Publication date:
2012

Design and performance of the collective Thomson scattering receiver at ASDEX Upgrade

V. Furtula, M. Salewski, F. Leipold, P. K. Michelsen,
S. B. Korsholm, F. Meo, D. Moseev, S. K. Nielsen, and M. Stejner
Association Euratom - Risø National Laboratory for Sustainable Energy, Technical University of Denmark, DK-4000 Roskilde, Denmark

T. Johansen
DTU Elektro, Technical University of Denmark, DK-2800 Lyngby, Denmark

(Dated: November 16, 2011)

Abstract

Here we present the design of the fast-ion collective Thomson scattering (CTS) receiver for millimeter wave radiation installed at ASDEX Upgrade, a tokamak for fusion plasma experiments. The receiver can detect spectral power densities of a few eV against the electron cyclotron emission (ECE) background on the order of 100 eV under presence of gyrotron stray radiation that is several orders of magnitude stronger than the signal to be detected. The receiver down-converts the frequencies of scattered radiation (100-110 GHz) to intermediate frequencies (IF) (4.5-14.5 GHz) by heterodyning. The IF signal is divided into 50 IF channels tightly spaced in frequency space. The channels are terminated by square-law detector diodes that convert the signal power into DC voltages. We present measurements of the transmission characteristics and performance of the main receiver components operating at mm-wave frequencies (notch-, bandpass-, and lowpass filters, a voltage-controlled variable attenuator, and an isolator), the down-converter unit, and the IF components (amplifiers, bandpass filters, and detector diodes). Furthermore, we determine the performance of the receiver as a unit through spectral response measurements and find reasonable agreement with the expectation based on the individual component measurements.

I. INTRODUCTION

Radiometers are remote sensing instruments that collect electromagnetic radiation in the millimeter and submillimeter wavelength range (30 GHz-3 THz) and measure its spectral power density. The collective Thomson scattering (CTS) receiver we discuss here is a radiometer designed to detect radiation in the frequency range 100-110 GHz by the principle of heterodyne detection. This is the expected Doppler-shift frequency range for gyrotron 105 GHz radiation scattered due to presence of fast ions up to 500 keV in the plasma at ASDEX Upgrade (AUG). Overviews of heterodyne methods used for plasma diagnostics are given in [1, 2].

CTS receivers have been used for a variety of measurements at several tokamaks and stellarators, for example at JET [3], W7-AS [4, 5], FTU [6, 7], TEXTOR [8–11], ASDEX Upgrade [12–14] or LHD [15]. Many parameters can be measured by CTS [16], for example the ion temperature [4] or the fuel ion ratio [17, 18]. The setup of the AUG CTS receiver presented here is designed to detect energetic particles [12–14]. The technical challenge is to design a radiometer that can detect spectral power densities of a few eV against the electron cyclotron emission (ECE) background on the order of 100 eV. To distinguish the CTS signal from the ECE background, the gyrotron is modulated using on/off periods. While the gyrotron is off, we measure the ECE radiation, and while the gyrotron is on, we measure the sum of ECE background and CTS signal. The difference between the two levels is the CTS signal. During the phases in which the gyrotron is on, one additionally has to deal with gyrotron stray radiation that is several orders of magnitude stronger than the signal to be detected. CTS, as well as other diagnostics using millimeter waves, is well-suited for the strongly radiative environments of ITER or future fusion reactors [19–21]. A CTS diagnostic has been enabled in ITER and will allow detection of the energy distribution of alpha particles in the burning plasma of ITER [22–24].

In this paper we will discuss the design and performance measurements of the main components of the CTS receiver installed on AUG. AUG is equipped with dual frequency 1 MW gyrotrons (105 GHz and 140 GHz) which are operated at 105 GHz for CTS experiments [25, 26]. The radiation from the gyrotron is launched into the plasma via a quasi-optical transmission line consisting of five reflectors and an electrically long, circular, overmoded waveguide. The receiver collects part of the scattered radiation via a similar

quasi-optical transmission line. After the quasi-optics the scattered radiation enters a circular horn antenna which is tapered down to a single-mode circular waveguide. Then we use a circular-to-rectangular waveguide converter to guide the radiation further into the heterodyne microwave receiver.

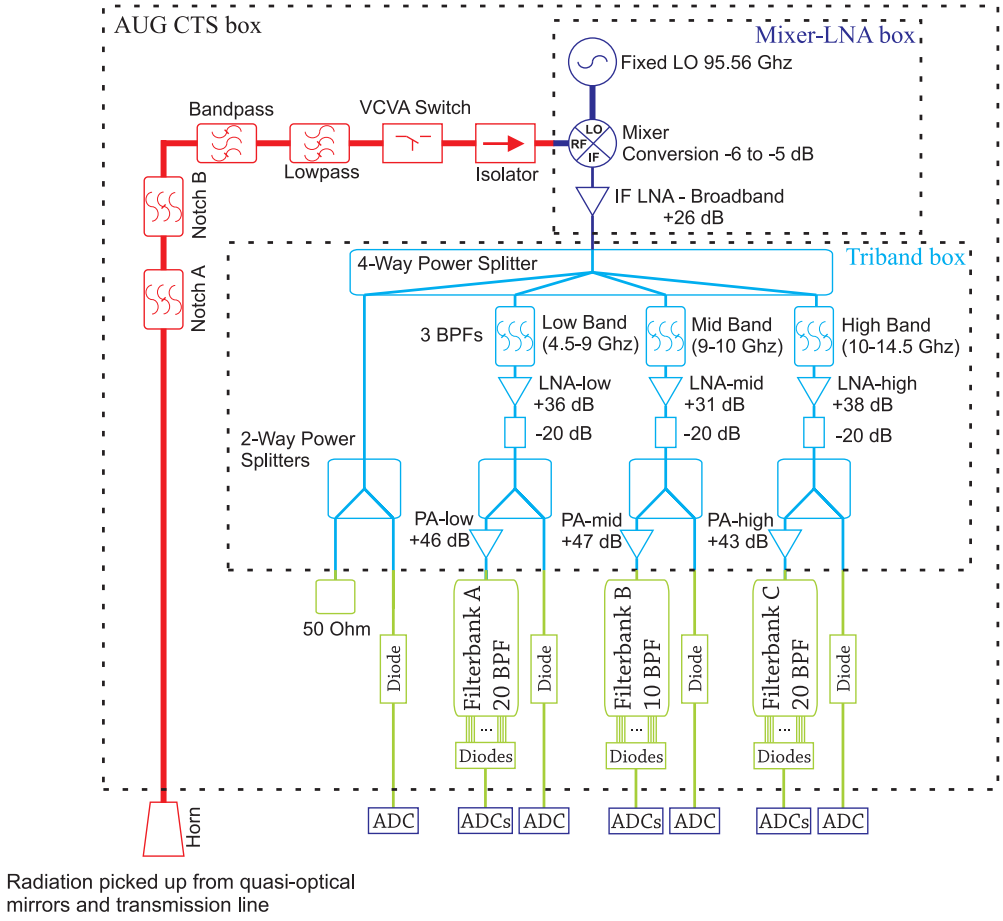

FIG. 1. Schematic of the AUG CTS receiver. The dashed lines represent shielding boxes in which the receiver components are installed. The RF line is shown in red; the mixer, the LO, and the broadband LNA in the mixer-LNA box are shown in dark blue; the components in the triband box are shown in blue; and the filterbanks A, B, and C and the detector diodes are shown in green.

A schematic of the AUG CTS receiver is shown in Fig. 1. All components are placed in an electrically shielded box, called "AUG CTS box" in Fig. 1. The radiation enters the horn antenna and passes through the RF line (red in Fig. 1) consisting of the horn antenna, two notch filters (General Atomic), a bandpass filter (ELVA-1, BPF-10/104/8), a lowpass filter (ELVA-1, LPF-10/112), a voltage controlled variable attenuator (ELVA-1, VCVA-10/105/2), and an isolator (ELVA-1, IF-10). Then the RF signal enters the mixing

stage where the signal is heterodyned to intermediate frequencies (IF). The local oscillator (LO, ELVA-1, CIDO-08/95.5/20), the mixer (ELVA-1, BM-08/95.5/14.5), and a wideband low-noise amplifier (LNA, Mini-Circuits, ZVA-183) are placed in a shielded compact copper box, called "Mixer-LNA box" (dark blue in Fig. 1), in order to screen out LO signals. The IF signal at the LNA output is divided using a four-way power divider and three bandpass filters into three frequency bands. Each of the three frequency bands is furthermore equipped with a cascade of two IF amplifiers, the first is an LNA (Miteq AFS4) and the second is a power amplifier (PA, Miteq-AFSD6). These components are located in a shielded box that is called "Triband box" shown in blue (Fig. 1). The fourth branch in the triband box is used for auxiliary purposes only. After the triband box the IF signal is fed to the filterbanks A (4.5 - 9 GHz), B (9 - 10 GHz), and C (10 - 14.5 GHz) and divided into a total of 50 channels using bandpass filters and power dividers. Filterbanks A and C have 20 channels each whereas filterbank B has 10 channels. In each channel, the power after the bandpass filter is converted to a DC voltage using a square-law detector diode. The voltage is recorded using a 24 bit analog-to-digital converter (ADC).

Before plasma discharges with CTS experiments, the receiver is calibrated. The receiver views eccosorb at liquid nitrogen temperature and at room temperature, giving two calibration points. If possible, a third calibration point can be taken by viewing a resonance in the plasma in X-mode. Here the plasma temperature must then be available from an independent measurement.

In the following we will discuss performance measurements of each component in the order the radiation encounters them on its way through the receiver: The notch filters, the bandpass and lowpass filters, the VCVA, and the isolator in the RF line (Sec. II), the mixer and the LNA in the mixer-LNA box (Sec. III), the power divider, bandpass filters, and amplifier chains in the triband box (Sec. IV), the filterbanks (Sec. V), and finally the diodes (Sec. VI). We will conclude with a measurement of the spectral response of the entire receiver and compare it with the expectation based on the individual component measurements (Sec. VII). Our conclusions are drawn in Sec. VIII.

II. COMPONENTS IN THE RF LINE

The RF line contains two notch filters in cascade, a bandpass and a lowpass filter, a VCVA, and an isolator (see Fig. 1). In this section we discuss these components. Radiation entering the RF line via the horn antenna encounters first two cascaded notch filters. Their stopband center frequency f_0 is tuned to the gyrotron frequency 104.95 GHz. Gyrotron stray radiation is suppressed whereas scattered radiation in the range 100-110 GHz passes on either side of the stopband [27–32]. The attenuation of each notch filter is more than 50 dB in the stopband as shown in Fig. II. The insertion loss is about 2 dB in most of the passband. We define insertion loss (IL) as the ratio between received (port 2) and inserted power (port 1) in dB, i.e. IL $= -20 \log_{10} |S_{21}|$ in terms of two-port S-parameters. This is the well-known S-parameter S_{21} with a negative sign. The attenuation of both notch filters is stronger for frequencies above 108 GHz, such that the attenuation at 110 GHz is about 10 dB. This is due to the selected cavity diameter and the ratio between the cavity diameter and the cavity length that place the cavity resonances close to the upper range of the desired passband ($\sim$110 GHz) and thereby introduce additional attenuation.

The 3 dB bandwidth of notch filter A is around 280 MHz and that of notch filter B is around 250 MHz. For a bandwidth of 130 MHz centered at 104.95 GHz, we find that the stopband attenuation is more than 54 dB for notch filter A and more than 52 dB for notch filter B. Due to the fact that the gyrotron probing beam is considerably stronger compared with ECE levels, we need two notch filters in cascade to damp the gyrotron stray radiation to the level of the ECE. High incoming power can saturate or even damage active components in the receiver. Radiation at the horn antenna is only a fraction of the available gyrotron power ($\sim$600 kW or 88 dBm), so if for example 0.1% (58 dBm) of the gyrotron power enters the horn antenna, the power at the output of notch filter B will be less than -48 dBm. Since a dynamic range more than 70 dB for signals in W-band is not easily measured with present network analyzers, we use two matched notch filters with stopband attenuation in the range 50 - 60 dB each to assure sufficient attenuation of the gyrotron stray radiation.

The next component along the RF line is the bandpass filter. Plasmas radiate in a wide range of frequencies, also below 100 GHz. As our LO frequency is about 95.5 GHz, radiation at 81 - 91 GHz will be mixed to the same IF frequencies as radiation at 100 - 110 GHz. The RF bandpass filter has a passband that covers the range 100-110 GHz but suppresses the

image response at 81 - 91 GHz more than 70 dB as shown in Fig. II. The bandpass filter has an opening (low damping) at around 140 GHz which is unfortunate since AUG plasmas are frequently heated by electron cyclotron resonance heating with gyrotrons at 140 GHz. A low-pass filter is installed in the RF line after the bandpass filter to block stray radiation from these 140 GHz gyrotrons. The transmission characteristic of the bandpass filter has also been measured. The attenuation at 140 - 200 GHz is more than 25 dB whereas the insertion loss at 100 - 110 GHz, the relevant frequencies for CTS, is in the range 2.5-3 dB. The cut-off frequency of the lowpass filter is 112 GHz.

The next component in the RF line is the VCVA. In CTS experiments the gyrotron is frequently modulated: 2 ms on / 2 ms off. During the switching phases the gyrotron chirps so that for a short time the gyrotron frequency, though at power levels much lower than maximum, is outside the stopband of the notch filters [13]. Gyrotron stray radiation would then bypass the notch filters and enter the receiver which could lead to gain compression of the IF amplifiers. We place a VCVA in front of the mixer to attenuate the signal during the gyrotron switching phases. While the VCVA is in closed mode, it will attenuate the input signal by approximately 40 dB. In the open mode the VCVA will introduce approximately 2 dB insertion loss (see Fig. II).

The last component in the RF line is the isolator which is used to damp back-reflections and prevent spurious signals, for example from the LO, from leaking back into the RF line. The isolator will minimize standing waves in the RF line at the cost of additional insertion loss that we measure to be in the range 1-2 dB.

We can calculate the transmission of the cascaded system from the individual component measurements by summing up the S-parameters of all components in the RF line. The results are presented in Fig. II. We used a linear summation of the component insertion loss (S_{21} in dB) because the return losses at connecting ports of each component are low, i.e S_{11} and S_{22} more than 15 dB are considered to be matched. We define return loss (RL) as the ratio between reflected and inserted power in dB, i.e. $\mathrm{RL}_{in,out} = -20\log_{10}|S_{11}| \approx -20\log_{10}|S_{22}|$ at input port 1 and output port 2, respectively. Such reflections are low since the connecting waveguide ports have the same dimensions implying that the characteristic impedance is the same. We therefore assume that we can predict transmission characteristics reliably if we just know S_{21}. In the passband range outside the deep notch, we measure an insertion loss of about 9 dB at frequencies below 108 GHz and up to 26 dB in the frequency range 108 -

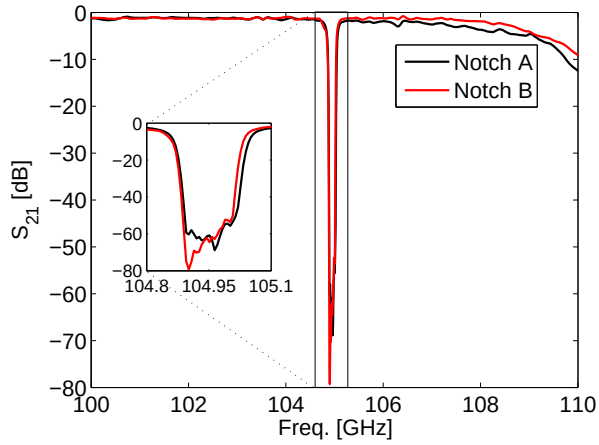

FIG. 2. Separate measurements of S_{21} of the two notch filters in the frequency range relevant to CTS experiments at ASDEX Upgrade (100 - 110 GHz).

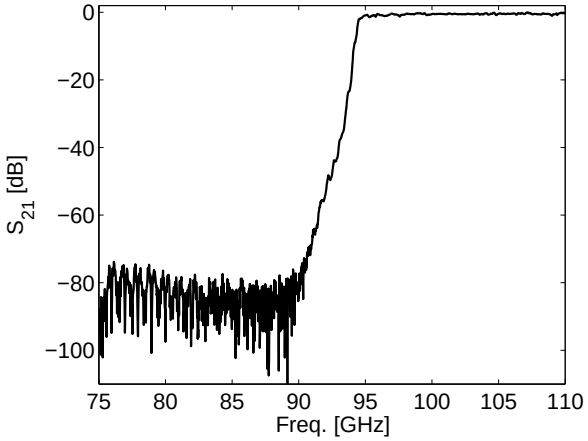

FIG. 3. Measurement of S_{21} of the bandpass filter in the frequency range relevant to CTS experiments and below. The bandpass filter attenuates at frequencies below 95 GHz.

110 GHz.

III. MIXER AND IF BROADBAND AMPLIFIER

After the isolator the radiation in the W-band range enters the mixer in the mixer-LNA box (Fig. 1). The mixer down-converts the radiation from W-band to the IF band. The IF is chosen at frequencies lower than the RF input since the sharpness of the IF filters determines how good different channels are separated in frequency. The mixer is pumped

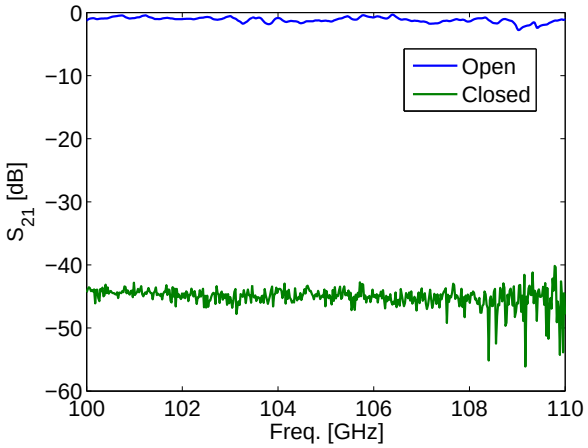

FIG. 4. Measurement of S_{21} of the VCVA in open and closed mode in the frequency range relevant to CTS experiments.

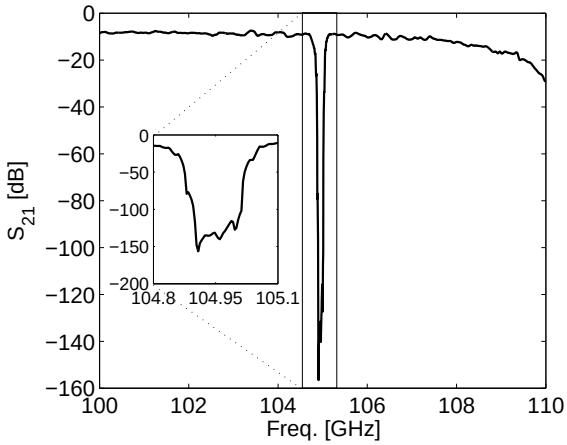

FIG. 5. Total insertion loss (S_{21}) of the RF line in the frequency range relevant to CTS experiments. The insertion loss is calculated from the individual RF component measurements.

by an IMPATT diode [33] LO at 95.51 GHz with 13 dBm output power. The RF input power where the 1-dB compression point appears at the IF output is around 0 dBm. The mixer conversion loss is defined as difference between output and input powers evaluated at the IF and RF ports, respectively. The conversion loss is measured using a frequency multiplier ($\times$ 6, i.e. at the sixth harmonic, RPG AFM6-110) driven by a signal generator (Rohde & Schwarz, SMR20), and the output power is measured at the IF port using a power meter (Agilent Technologies, E4416A). The measurements are presented in Fig. 6. We find the conversion loss to be almost constant in the range 5 dB to 6 dB for the RF input in the

range 100 - 110 GHz. The isolator will partly prevent LO self-mixing since any fraction of the LO signal leaking into the RF port will to a large part be absorbed in the isolator. Any unabsorbed part will be reflected back into the mixer RF port causing DC signals at the IF output port. Therefore a DC-block is integrated at the IF port of the mixer.

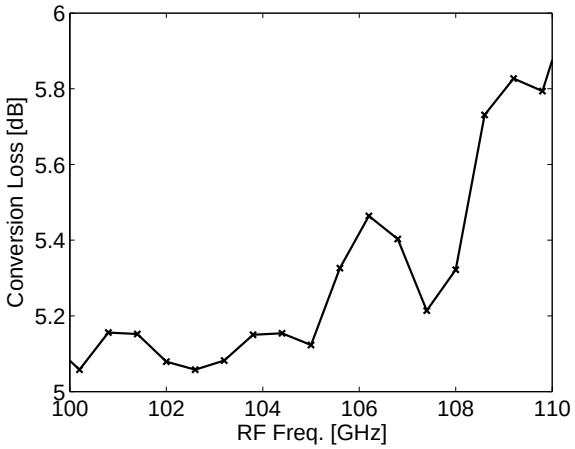

FIG. 6. Mixer conversion loss in the frequency range relevant to CTS experiments.

In order to reduce the receiver noise figure (NF), an IF broadband amplifier is placed right after the mixer IF port in the mixer LNA-box and is the first stage of amplification. It covers the full CTS IF spectrum from 4.5 to 14.5 GHz with amplification of about 26 dB as shown in Fig. 7. The amplifier gain has been tested for several input powers for the frequency range from 2 to 15 GHz and is confirmed to vary only by 1 to 2 dB in all cases. The noise figure is in the range from 3.0 to 5.5 dB. The 1 dB compression point is about 0 dBm input power which is orders of magnitude higher than the power expected during CTS experiments.

The broadband amplifier is expected to operate linearly in the IF range from 4.5 to 14.5 GHz. However, second harmonics generated from signals between 4.5 and 7.25 GHz can erroneously be interpreted as CTS signals between 9 and 14.5 GHz. Therefore the generation of second harmonics has been measured for various input power levels, as seen in Fig. 8. The second harmonic is suppressed by more than 40 dB (relative to the fundamental) at low frequencies (2 to 6 GHz) and low input powers (-30 to -15 dBm). At high frequencies (8 - 12 GHz) and high input powers (-10 to 0 dBm), the suppression is more than 25 dB, but the frequency range of the second harmonics (16-24 GHz) is outside the reception spectrum of the receiver and does not interfere with the CTS signal. Input power higher than -30 dBm

is unlikely during CTS experiments, so we expect to have at least 45 dB suppression of the second harmonic in the IF frequency range.

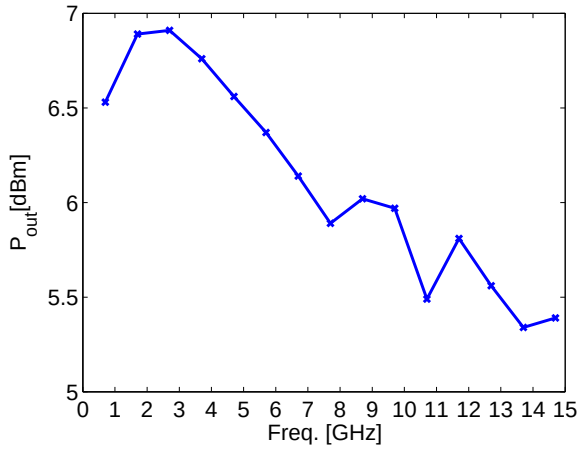

FIG. 7. Measured output power spectrum of the IF amplifier for an input power of $P_{in} = -20\ dBm$.

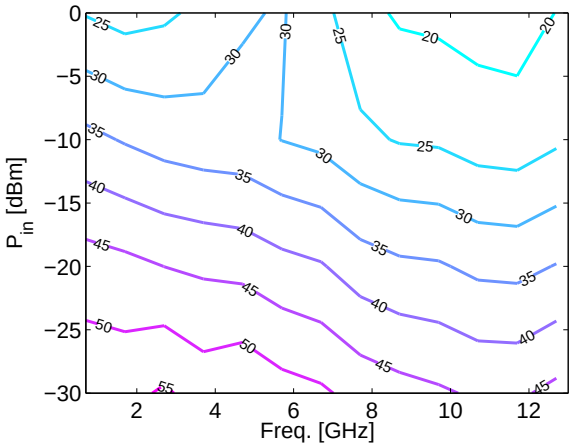

FIG. 8. The second harmonic generated at various frequencies and input powers. The isocontours represent the ratio of the power between second harmonic and fundamental at the output in dB.

We can determine the total noise factor F_{chain} from the horn antenna to the output of the IF broadband amplifier and further to the four-way power divider using Friis' formula [34] for cascaded two-port devices.

$$F_{chain} = F_1 + \frac{F_2 - 1}{G_{av,1}} + \frac{F_3 - 1}{G_{av,1}G_{av,2}} + \dots \tag{1}$$

where F_1 is the noise factor of stage 1 and $G_{av,1}$ is the available power amplification from stage 1 and similarly for stage 2, 3 and further on. The terms on the right-hand-side of

Eq. (1) are expressed in linear scale. The noise factor of the RF line together with the mixer (RF to IF), F_1, is equal to the system loss, i.e. for passive components $F_1 = G_{av,1}^{-1}$. F_2 and $G_{av,2}$ represent the noise factor and available gain of the broadband LNA, respectively. F_3 is the loss of the four-way power divider discussed in Sec. IV. Eq. (1) can be simplified to

$$F_{chain} = F_1 F_2 + \frac{F_1(F_3 - 1)}{G_{av,2}} + \ldots \approx F_1 F_2. \tag{2}$$

When the noise factor F_{chain} is converted to dB by $\mathrm{NF}_{dB} = 10 \log_{10} F_{chain}$, we refer to it as noise figure.

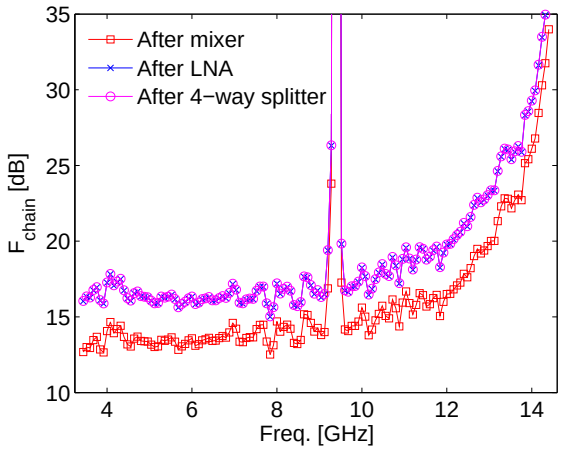

FIG. 9. Noise figures of the cascade from the horn antenna to various places along the transmission line. The noise figures after the LNA and after the four-way power divider are very similar.

Figure 9 shows the noise figures at various points along the transmission line: after the mixer, after the LNA, and after the four-way power divider. The total noise figure F_{chain} is very similar before and after the four-way power divider and in fact at any other place in the transmission line thereafter. F_{chain} is dominated by the losses in the RF line (F_1) times the noise figure of the LNA (F_2), as Eqn. (2) also shows. The IF broadband amplifier is placed right after the mixer, so that the contribution to the receiver noise figure of all IF components further down the transmission line is as low as possible. This will lead to the optimum noise figure for the entire system.

IV. TRIBAND BOX

After the IF radiation has passed the first stage of amplification, it enters the triband box which splits and further amplifies the IF signal as shown in Fig. 1. The first component in the triband box is the four-way power divider leading to three branches consisting of each a bandpass filter (Micro-Tronics) and a two-stage amplifier chain. The fourth branch is used for auxiliary measurements. The insertion loss of the four-way power divider is in the range from 6.5 to 7.5 dB over the frequency range 4.5 to 14.5 GHz. The insertion loss covers the inevitable loss of 6.0 dB due to four-way power splitting and 0.5 to 1.5 dB due to frequency dependent loss in the microstrip lines. The triband box splits the radiation into three frequency bands; a low band (4.5 - 9 GHz), a mid band (9 - 10 GHz), and a high band (10 - 14.5 GHz). The selection is made by a lowpass and two bandpass filters with insertion and return losses shown in Figs. 10-12. The filters have good selectivity, low insertion loss in the passband, and broad rejection bandwidth.

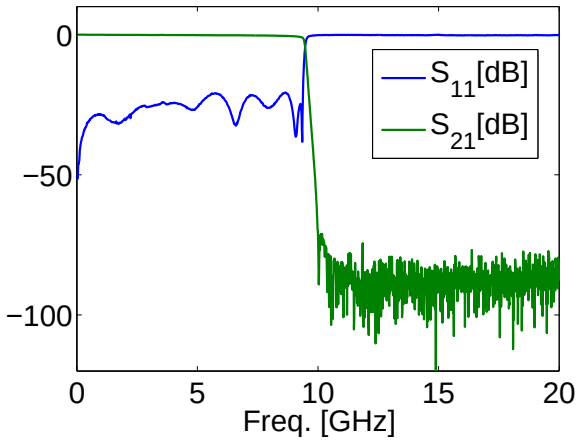

FIG. 10. Insertion loss and return loss of the bandpass filter in filterbank A (4.5 - 9 GHz).

The main reason for dividing the receiver line into three separate frequency bands is the different spectral power density ranges of the detected radiation. We expect larger spectral power densities in the range ±500 MHz around the gyrotron frequency corresponding to scattering from bulk ions. Therefore our mid branch is 1 GHz wide while the two neighbor branches, where less radiation is expected, are each 4.5 GHz wide to cover the expected CTS frequency range. Another advantage of dividing CTS band into 3 sub-bands is channel protection of the low and high branches in the case of strong gyrotron stray radiation. That

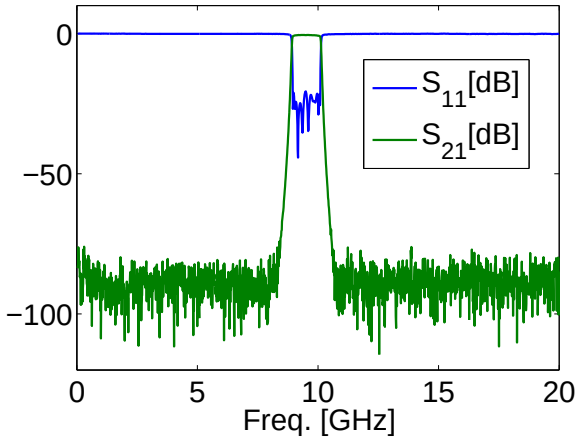

FIG. 11. Insertion loss and return loss of the bandpass filter in filterbank B (9 - 10 GHz).

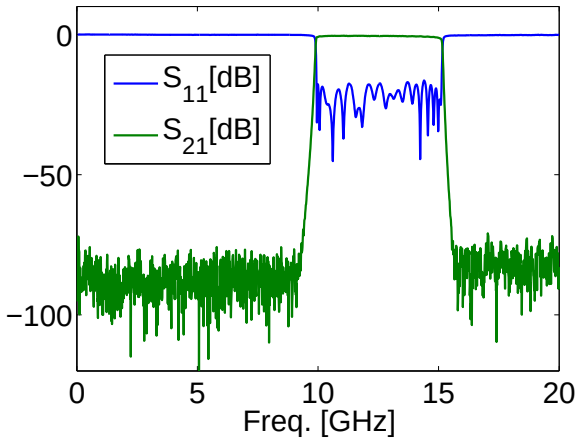

FIG. 12. Insertion loss and return loss of the bandpass filter in filterbank C (10 - 14.5 GHz).

way only the mid branch is at risk to saturate while the low and high branches will be unaffected assuming the mixer is not saturated. The attenuators shown in Fig. 1 in each of the three bands are used to adjust the signal levels and to prevent standing wave arising between the amplifiers.

We investigate the linearity of the amplification in the triband box at different frequencies (Figs. 13-15). Since the slopes of the curves in Figs. 13-15 are unity, the response of the triband box is linear for input powers up to -40 dBm evaluated at several frequencies of interest in each of the three bands. Figure 16 shows the gain of the triband box in the IF frequency range (4.5 to 14.5 GHz) for an input power of -60 dBm. The low band is relatively flat with a gain in the range from 36 to 39 dB; the mid band is reduced in bandwidth due

to the bandpass filter and has a gain in the range from 47 to 48.5 dB; and the high band has the largest gain variation in the range from 46.5 to 54 dB.

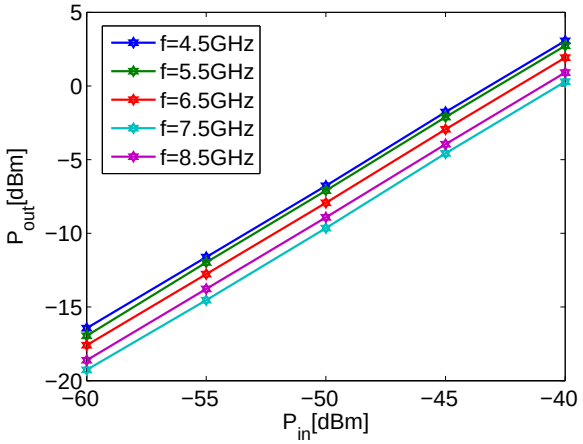

FIG. 13. Output power versus input power for various frequencies for the amplifiers in filterbank A.

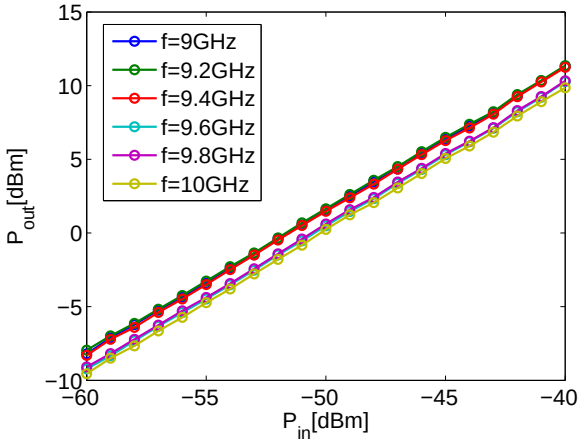

FIG. 14. Output power versus input power for various frequencies for the amplifiers in filterbank B.

Electrical properties of the seven amplifiers in the receiver are shown in Tab. I. In case we receive a broadband signal with increasing power level at the horn antenna, the components will saturate in the following order: the three PA's right before filterbanks A, B, and C, the three LNA's driving the PA's, the mixer, and finally the broadband LNA driven by the mixer. These results are found by calculating the power budget at the input port of each component.

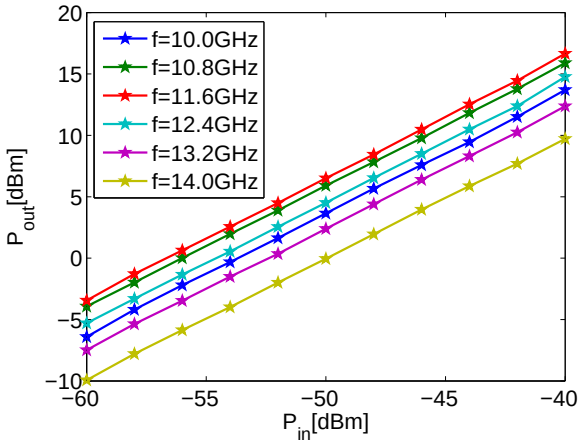

FIG. 15. Output power versus input power for various frequencies for the amplifiers in filterbank C.

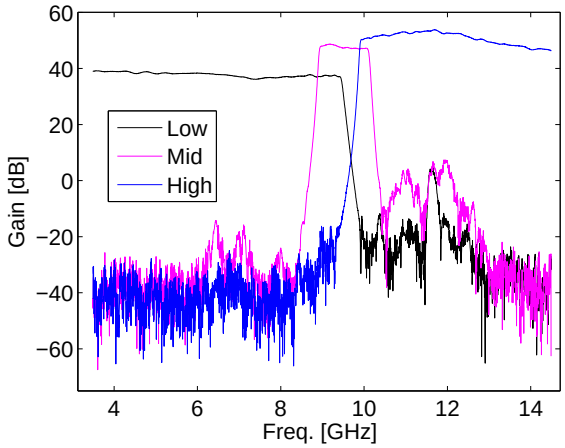

FIG. 16. Gain of the triband box measured with a network analyzer. The test input power is -60 dBm. The signal is split into the three frequency bands given by the bandpass filters discussed in Figs. 10-12.

V. FILTERBANKS

The three IF branches leaving the triband box enter the filterbanks A, B, and C. The three filterbanks consist of power dividers, jumpers, and bandpass filters that are used to obtain tightly spaced channels in frequency space. The bandpass filters have relatively sharp roll-off attenuation in the range 0.1-0.15 dB/MHz and a passband insertion loss in the range 0.2 - 0.6 dB. Filterbank A has 20 channels (4.5 - 9 GHz), filterbank B 10 channels (9 - 10 GHz),

	Freq. [GHz]		Gain [dB]		Max output power [dBm]		Noise Figure [dB]	
	f_l	f_u	Min	Max	Min	Max	Min	Max
LNA-broadband	0.7	18	24	26	21	24	3.0	5.5
LNA-lowband	3	9	35.2	36.2	15.6	17.2	1.25	1.98
LNA-midband	9	10	30.4	31.1	15.1	16.5	0.92	1.31
LNA-highband	10	16	35.23	38.08	15.21	16.56	1.29	1.74
PA-lowband	3	9	42.5	46.1	25.2	26.7	3.34	4.97
PA-midband	9	10	45.7	47.7	25.3	26.0	1.27	1.30
PA-highband	10	16	40.46	43.19	24.19	24.42	3.29	3.59

TABLE I. Amplifier specifications. The maximum output power is defined at the 1 dB gain compression point. f_l and f_u represent the lower and upper frequencies of operation, respectively.

and filterbank C 20 channels (10 - 14.5 GHz). The channels are numbered consecutively from 1 to 50 in the order of ascending channel center frequency. The attenuation at the center frequency across all channels varies from 10 to 20 dB due to different types of power dividers needed to split the signal in the three main branches into 50 channels. However, the attenuation level across the channels is approximately symmetric about channel 25, which also ensures a spectral balance on each side of the notch filter during liquid nitrogen calibration. The spectral resolution in channels 6 to 45 is 100 MHz. In the outer channels larger bandwidths are chosen to increase the signal-to-noise ratio, i.e. bandpass filters with 3-dB bandwidths of around 500 MHz are used in channels 2-5 and 46-49 and of around 1.1 GHz in channels 1 and 50.

We have measured all microwave components from the horn antenna down to the output ports of the bandpass filters in the 50 channels. Using this measured data we can calculate the gain through the CTS receiver. Figures 17-19 shows the gain for a few representative channels in their relevant frequency ranges. The suppression of radiation at frequencies outside their prescribed passbands is more than 70 dB.

VI. SQUARE-LAW DETECTOR DIODES

The final stage of our interest in the AUG CTS receiver are the square-law Schottky detector diodes (Herotek, High sensitivity zero bias Schottky detectors) that are connected

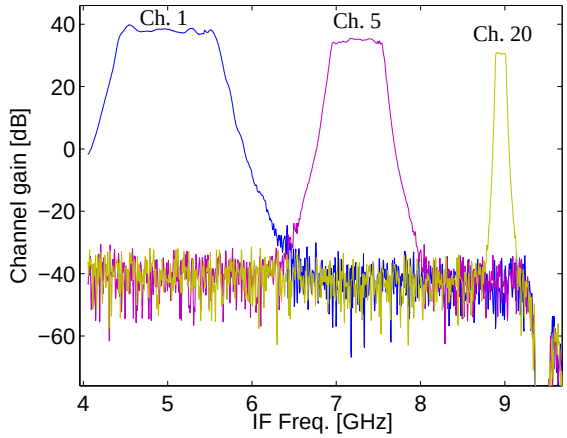

FIG. 17. Calculated gain from the horn to the output port of bandpass filters for a few representative channels in filterbank A.

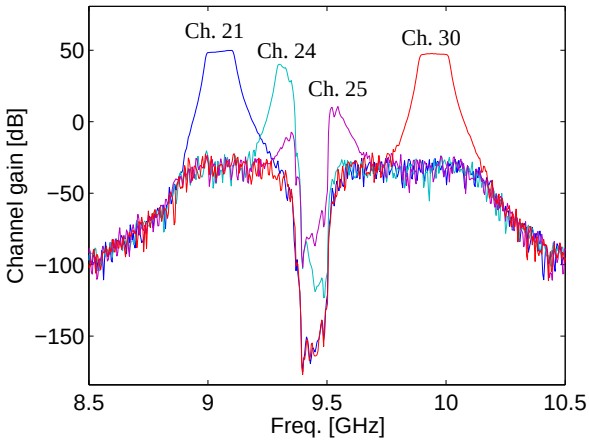

FIG. 18. Calculated gain from the horn to the output port of bandpass filters for a few representative channels in filterbank B.

to each of the 50 IF channels. The diodes transform the IF signal to a DC level which is then amplified by a factor 60 using operational DC amplifiers and afterwards recorded using ADC cards (National Instruments 4472). The ADC cards accept voltages from -10 V to 10 V giving 20 V in total dynamic range. The theoretical voltage resolution is $V_{ADC} = 20/2^{23}\ V \sim 2.38\ \mu V$ which is far below the noise level detected during liquid nitrogen calibration. Since the square-law diodes have negative output polarity, we only use half of the total dynamic range, i.e. from -10 V to 0 V. The power-voltage characteristics of the diodes are shown in Figs. 20-21. The diodes are tested using a signal generator at the

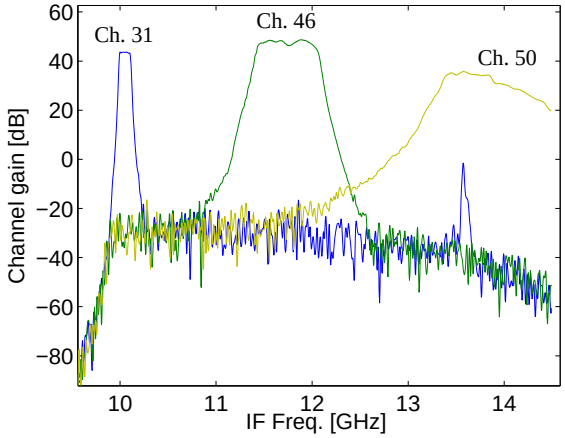

FIG. 19. Calculated gain from the horn to the output port of bandpass filters for a few representative channels in filterbank C.

frequency that corresponds to the channel number at the IF input port. The power of the signal generator is swept in power from -40 dBm to 0 dBm in 1 dB steps, and the voltage at the output is measured with a voltmeter. Fig. 20 presents the output voltage, U_{out}, as a function of input power, P_{in}.

Fig. 21 shows that the values of the gradient $-\mathrm{d}U_{out}/\mathrm{d}P_{in}$ are in the range from 300 to 3000 V/W for input powers from 0 to -40 dBm. These gradients are also called diode sensitivities. For powers below -20 dBm, the diodes operate in the square-law region with approximately constant sensitivity of around 1000 V/W for all the channels except 42, 44 and 46. For powers more than -20 dBm, the diodes operate in the resistive region where the sensitivity decreases down to 300 V/W for 0 dBm power input. The diodes in channels 42, 44 and 46 have sensitivities as high as 3000 V/W which are taken into consideration during receiver calibration.

We can estimate the output voltage with good accuracy for arbitrary power in the range between -40 dBm and 0 dBm. For low power input, < -30 dBm, we get uncertainties in the voltmeter readout up to 0.1 mV. If the signal is lower (<-40 dBm), which would be the case in most channels during CTS experiments, we extrapolate the diode output based on the measured data assuming that in this range the response should be linear. The slope of the line is now determined as the intercept point with the y-axis is set to zero since the diode voltage is zero for zero input power.

Since we can record signals in the voltage range -10 to 0 V and have $\times$ 60 DC amplification,

the output voltage signals right after the diodes are in the range -0.167 to 0 V. A voltage level of -0.167 V corresponds to an input power in the range -9 to -7 dBm according to Fig. 20 which is far inside the resistive region of the diodes according to Fig. 21. Since the square-law region for all the diodes is below -20 dBm, the output voltage U_{out} is in the range -30 to -10 mV which after DC amplification becomes -1.8 to -0.6 V. Therefore the recorded voltage at the ADC's should not be lower than -1.8 V, so the square-law Schottky diode characteristics are in their desired operation ranges.

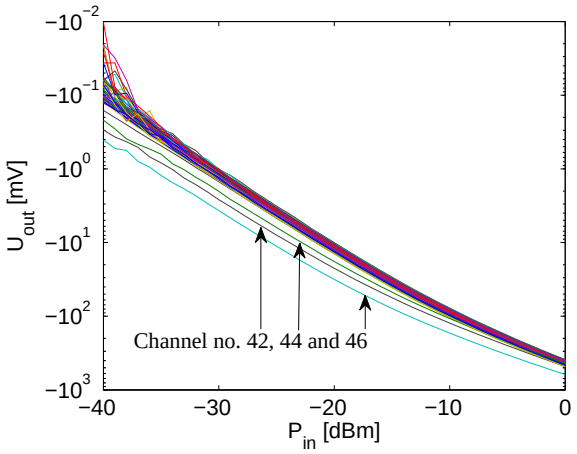

FIG. 20. Voltage-power characteristic of 50 square-law detector diodes terminating the 50 receiver channels.

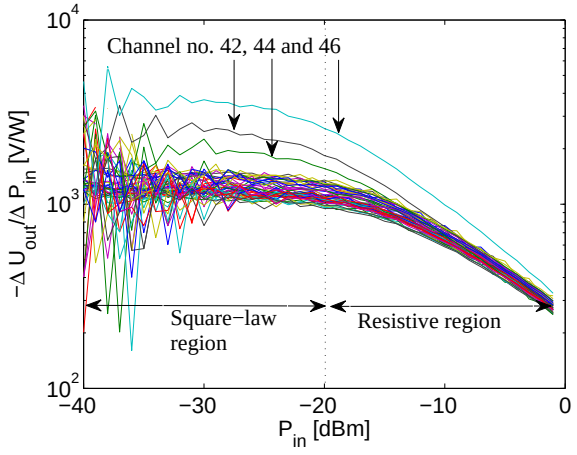

FIG. 21. Slope of the voltage-power characteristic versus input power of the 50 square-law detector diodes.

VII. CHARACTERIZATION OF THE RECEIVER

The receiver performance can be investigated by applying a single frequency signal at the input of the RF line and measuring the output at the 50 ADC channels. We use a setup with a frequency multiplier, a signal generator, and two variable attenuators to construct a tunable RF signal source. The frequency multiplier is driven by a signal generator used in the range from 16 to 18.5 GHz in 2.5 MHz steps. The multiplier outputs are single frequency signals in the range 96 to 111 GHz in 15 MHz steps with a total power varying from 4 to 6 dBm. The output power from the frequency multiplier is too high for testing purposes, so we need to attenuate it with at least 50 dB before it enters the RF line. For this purpose we use two attenuators, the first one (Hughes) is tunable while the second (Flann) is set to maximum attenuation. We performed separate calibrations since W-band attenuators are not necessarily linear for each frequency or setting option. The experimental setup is shown in Fig. 22. During the experiment we vary the signal power by using the variable attenuator (Hughes) and the frequency by tuning the signal generator, and we record the readings on the ADC's at each channel.

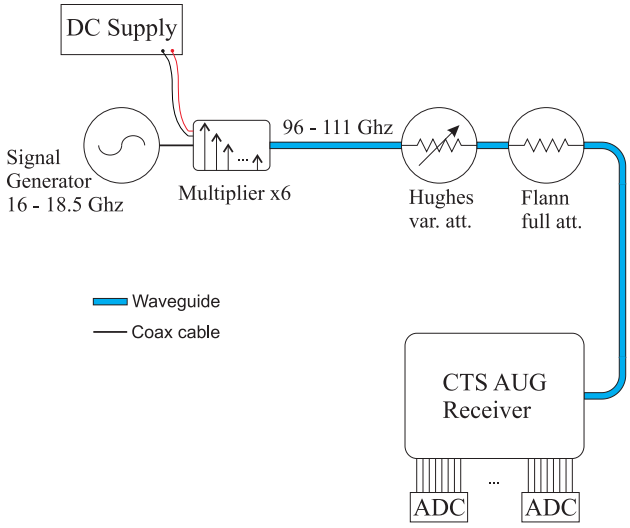

FIG. 22. Measurement setup to determine the frequency response of the CTS receiver.

We show the global frequency response of the CTS receiver at one power level, here -55 dBm, and measure the ADC voltages as function of the multiplier frequency. Figures 23 and 24 present the measurements and the corresponding expectation based on the measurements of the individual components, respectively. To calculate the expectation, we

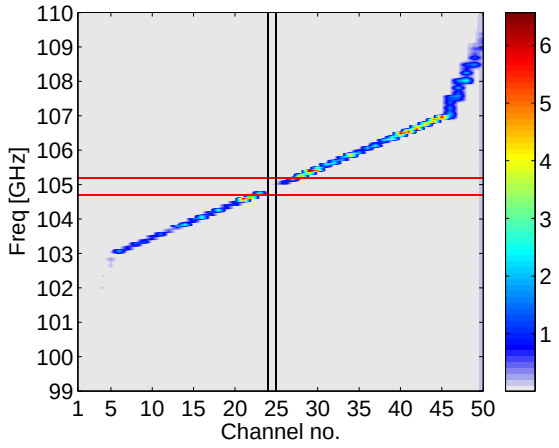

FIG. 23. Measured frequency response of the CTS receiver using the frequency multiplier with an almost fixed power of -55 dBm. The channels containing the notch (24 and 25) are emphasized as vertical black lines and the notch filter 3 dB bandwidth limits are shown as red horizontal lines.

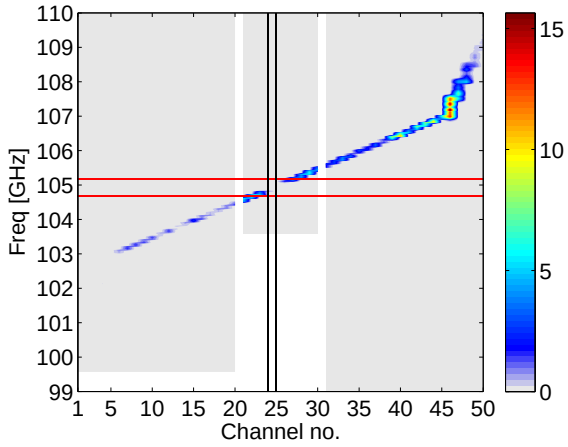

FIG. 24. Calculated frequency response of the CTS receiver corresponding to the measurement presented in Fig. 23.

disassembled the receiver and measured the transmission characteristics (S-parameters) of each component in the transmission line. The entire receiver as a unit was measured after it has been assembled again. Each channel only has a voltage response at its design frequency, indicating that the filters have proper attenuation outside their design passbands. Different color shades along the CTS channels show that they do not have a flat frequency response, corresponding to the transfer characteristics shown in Figs. 17-19.

A second way to characterize the receiver is to increase the power and monitor the

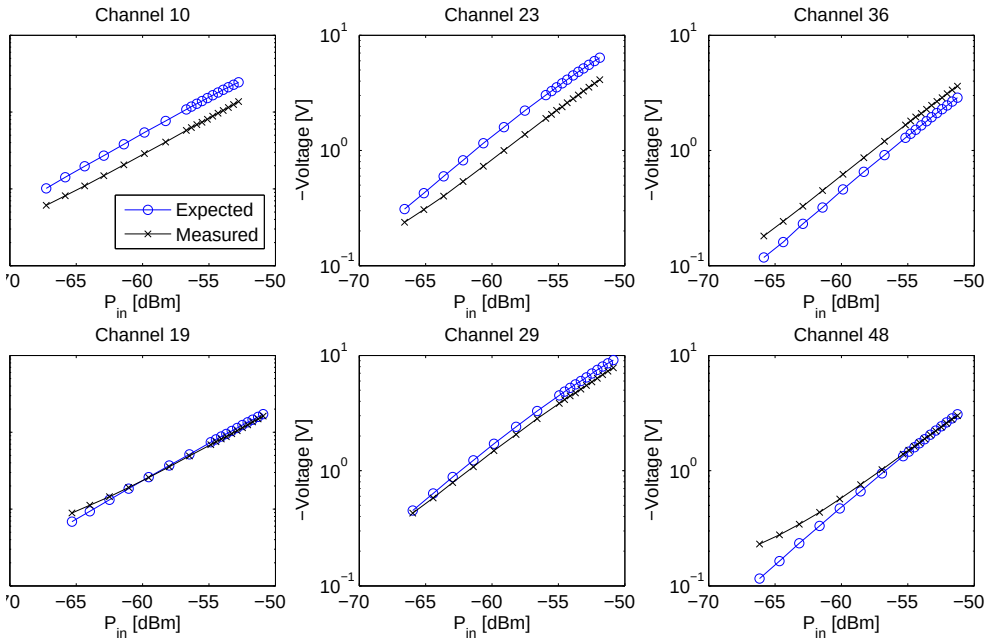

FIG. 25. Voltage-power characteristic of a few representative receiver channels with measurements in black and calculations based on individual component measurements in blue.

response of the 50 channels. Here we show data for a few representative channels: channels (10,19), (23,29), and (36,48) from filterbanks A, B, and C, respectively. The channel voltages are shown as function of signal power in Fig. 25. The measured voltage values are higher up to 5 times compared with expected voltage values for low RF power inputs. For higher power inputs (>-55 dBm) the ratio between the measured and expected voltage values, $\frac{V_{measured}}{V_{expected}}$, varies in the range 0.7 - 3.5.

The sensitivity (Volts per nanowatt, V/nW) of each channel as function of power can be found from the derivatives of the curves presented in Fig. 25. Most of the presented channels are linear and therefore have constant sensitivity as function of input power. The sensitivities of the different channels in the CTS receiver are in the range 0.5 to 3 V/nW for power inputs in the range -70 to -50 dBm.

VIII. CONCLUSIONS

The individual components of the CTS receiver at ASDEX Upgrade and their performance characteristics are presented. The receiver uses a heterodyne scheme, i.e. converts

signals in the W-band down to IF signals in a down-mixing stage. We find losses in the range 10 to 26 dB in the receiver RF line which is sometimes inevitable due to filtering requirements. The mixer has conversion losses in the range from 5 to 6 dB which adds to the receiver noise figure. The down-converted IF signal is amplified and divided into three bands using three bandpass filters in the triband box. There are two further amplifiers in each branch of the triband box, making it seven amplifiers in total. Thereby every branch has three amplifiers in cascade of which the first one is common for all three branches. The amplifiers have gain in the range from 24 to 46 dB and power output at 1 dB gain compression from 15 to 27 dBm. The IF filterbanks A, B, and C containing 50 bandpass filters will assure passage of signals in the frequency range from 4.5 to 14.5 GHz, each channel only in its design frequency bandwidth of typically 100 MHz. Schottky square-law detector diodes are used to convert the IF signal down to DC voltage levels which are acquired by 24 bit acquisition cards. The diodes operate in the square-law region for input powers up to -20 dBm. Their sensitivity in this region varies from 900 to 1300 V/W. The total receiver noise figure is frequency dependent and in the range between 11 and 20 dB except for in the notch filter channels. The largest contributions to the noise figure are the losses in the RF-line and the mixer conversion loss.

The characterization of the individual components allows us to calculate the receiver response to RF signals at various frequencies. This expectation of the receiver response is compared with the measured receiver response. To measure the entire receiver response, we use a signal generator and a frequency multiplier as a tunable single frequency signal source and a variable attenuator to control the output power. A scan with varying RF frequency and power has been performed. The measurement of the entire receiver response agrees reasonably well with the expectation based on the individual component measurements within a factor of about 3.5. In both measurement methods we find that the voltage response across channels is not flat and can vary by several volts. Generation of harmonics in the mixer or amplifiers and radiation leakage are well suppressed in the present CTS receiver design.

We have calculated the sensitivity as function of input power for all 50 channels for measurements as well as for the expectations. For the channels with low amplification, the sensitivity is relatively constant. For most of the channels, we find that the sensitivity is in the range from 0.5 to 3 V/nW for the measurements and expectations. With these

results we find it acceptable to use individual component measurements to predict the overall performance of the CTS AUG receiver.

ACKNOWLEDGMENTS

This work, supported by the European Communities under the contract of Association between EURATOM / Risø DTU, was partly carried out within the framework of the European Fusion Development Agreement. The views and opinions expressed herein do not necessarily reflect those of the European Commission.

---

[1] H. J. Hartfuss, T. Geist, and M. Hirsch, Plasma Phys. Control. Fusion, **39**, 1693 (1997).

[2] N. C. Luhmann, H. Bindslev, H. Park, G. Taylor, J. Sanchez, and C. Yu, Fusion Sci. Tech., **53**, 335 (2008).

[3] H. Bindslev, J. A. Hoekzema, J. Egedal, J. A. Fessey, T. P. Hughes, and J. S. Machuzak, Phys. Rev. Lett., **83**, 3206 (1999).

[4] E. V. Suvorov, V. Erckmann, E. Holzhauer, W. Kasparek, Y. A. Dryagin, S. E. Filchenkov, A. A. Fraiman, T. Geist, M. Kick, L. M. Kukin, A. V. Kostrov, L. V. Lubyako, A. M. Shtanyuk, N. K. Skalyga, and O. B. Smolyakova, Plasma Phys. Control. Fusion, **37**, 1207 (1995).

[5] E. V. Suvorov, E. Holzhauer, W. Kasparek, L. V. Lubyako, A. B. Burov, Y. A. Dryagin, S. E. Filchenkov, A. A. Fraiman, L. M. Kukin, A. V. Kostrov, D. A. Ryndyk, A. M. Shtanyuk, N. K. Skalyga, O. B. Smolyakova, V. Erckmann, T. Geist, M. Kick, H. Laqua, M. Rust, W7-AS Team, ECRH Team, and NBI Team, Plasma Phys. Control. Fusion, **39**, B337 (1997).

[6] U. Tartari, G. Grosso, G. Granucci, L. V. Lubyako, A. G. Shalashov, E. V. Suvorov, F. P. Orsitto, A. Simonetto, S. Nowak, F. Volpe, A. Bruschi, F. Gandini, V. Muzzini, S. Garavaglia, and G. Grossetti, Nucl. Fusion, **46**, 928 (2006).

[7] U. Tartari, G. Grosso, G. Granucci, F. Gandini, S. Garavaglia, G. Grossetti, A. Simonetto, V. Mellera, V. Muzzini, L. Lubyako, A. Shalashov, F. P. Orsitto, G. Ciccone, and F. Volpe, Rev. Sci. Instrum., **78**, 043506 (2007).

[8] D. Moseev, F. Meo, S. B. Korsholm, T. Koskela, M. Albergante, O. Asunta, H. Bindslev, A. Buerger, V. Furtula, M. Y. Kantor, F. Leipold, P. K. Michelsen, S. K. Nielsen, M. Salewski,

O. Schmitz, M. Stejner, E. Westerhof, and TEXTOR Team, Plasma Phys. Control. Fusion, **53**, pp.105004 (2011).

[9] S. K. Nielsen, H. Bindslev, M. Salewski, A. Burger, E. Delabie, V. Furtula, M. Kantor, S. B. Korsholm, F. Leipold, F. Meo, P. K. Michelsen, D. Moseev, J. W. Oosterbeek, M. Stejner, E. Westerhof, P. Woskov, and TEXTOR Team, Plasma Phys. Control. Fusion, **52**, 092001 (2010).

[10] S. K. Nielsen, M. Salewski, H. Bindslev, A. Burger, V. Furtula, M. Kantor, S. B. Korsholm, H. R. Koslowski, A. Kraemer-Flecken, F. Leipold, F. Meo, P. K. Michelsen, D. Moseev, J. W. Oosterbeek, M. Stejner, E. Westerhof, and TEXTOR Team, Nucl. Fusion, **51**, 063014 (2011).

[11] E. Westerhof, S. K. Nielsen, J. W. Oosterbeek, M. Salewski, M. R. De Baar, W. A. Bongers, A. Bürger, B. A. Hennen, S. B. Korsholm, F. Leipold, D. Moseev, M. Stejner, and D. J. Thoen, Phys. Rev. Lett., **103**, 125001 (2009).

[12] F. Meo, H. Bindslev, S. B. Korsholm, V. Furtula, F. Leipold, P. K. Michelsen, S. K. Nielsen, M. Salewski, J. Stober, D. Wagner, F. Leuterer, and P. Woskov, Rev. Sci. Instrum., **79**, 10E501 (2008).

[13] F. Meo, M. Stejner, M. Salewski, H. Bindslev, T. Eich, V. Furtula, S. B. Korsholm, F. Leuterer, F. Leipold, P. K. Michelsen, D. Moseev, S. K. Nielsen, B. Reiter, J. Stober, D. Wagner, P. Woskov, and ASDEX Upgrade team, J. Phys.: Conf. Series, **227**, 012010 (2010).

[14] M. Salewski, F. Meo, M. Stejner, O. Asunta, H. Bindslev, V. Furtula, S. B. Korsholm, T. Kurki-Suonio, F. Leipold, F. Leuterer, P. K. Michelsen, D. Moseev, S. K. Nielsen, J. Stober, G. Tardini, D. Wagner, P. Woskov, and ASDEX Upgrade team, Nucl. Fusion, **50**, 035012 (2010).

[15] S. Kubo, M. Nishiura, K. Tanaka, T. Shimozuma, Y. Yoshimura, H. Igami, H. Takahash, T. Mutoh, N. Tamura, Y. Tatematsu, T. Saito, T. Notake, S. B. Korsholm, F. Meo, S. K. Nielsen, M. Salewski, and M. Stejner, Rev. Sci. Instrum., **81**, 10D535 (2010).

[16] S. B. Korsholm, H. Bindslev, V. Furtula, F. Leipold, F. Meo, P. K. Michelsen, D. Moseev, S. K. Nielsen, M. Salewski, and M. Stejner, Nucl. Instr. and Methods in Phys. Res., **623**, 677 (2010).

[17] S. B. Korsholm, M. Stejner, H. Bindslev, V. Furtula, F. Leipold, F. Meo, P. K. Michelsen, D. Moseev, S. K. Nielsen, M. Salewski, M. de Baar, E. Delabie, M. Kantor, and A. Bürger, Phys. Rev. Lett., **106**, pp.165004 (2011).

[18] M. Stejner, S. B. Korsholm, S. K. Nielsen, M. Salewski, H. Bindslev, V. Furtula, F. Leipold, P. K. Michelsen, F. Meo, and D. Moseev,.

[19] M. Salewski, F. Meo, H. Bindslev, V. Furtula, S. B. Korsholm, B. Lauritzen, F. Leipold, P. K. Michelsen, S. K. Nielsen, and E. Nonbøl, Rev. Sci. Instrum., **79**, 10E729 (2008).

[20] F. Meo, H. Bindslev, S. B. Korsholm, E. L. Tsakadze, S. B. Korsholm, P. Woskov, C. I. Walker, and G. Vayakis, Rev. Sci. Instrum., **75**, 3585 (2004).

[21] F. Leipold, V. Furtula, M. Salewski, H. Bindslev, S. B. Korsholm, F. Meo, P. K. Michelsen, D. Moseev, S. K. Nielsen, and M. Stejner, Rev. Sci. Instrum., **80**, 093501 (2009).

[22] M. Salewski, S. K. Nielsen, H. Bindslev, V. Furtula, N. N. Gorelenkov, S. B. Korsholm, F. Leipold, F. Meo, P. K. Michelsen, D. Moseev, and M. Stejner, Nucl. Fusion, **51**, pp.083014 (2011).

[23] M. Salewski, O. Asunta, L.-G. Eriksson, H. Bindslev, V. Hynönen, S. B. Korsholm, T. Kurki-Suonio, F. Leipold, F. Meo, P. K. Michelsen, S. K. Nielsen, and J. Roenby, Plasma Phys. Control. Fusion, **51**, pp.035006 (2009).

[24] M. Salewski, L.-G. Eriksson, H. Bindslev, S. B. Korsholm, F. Leipold, F. Meo, P. K. Michelsen, and S. K. Nielsen, Nucl. Fusion, **49**, 025006 (2009).

[25] D. Wagner, G. Grünwald, F. Leuterer, A. Manini, F. Monaco, M. Münich, H. Schütz, J. Stober, H. Zohm, T. Franke, M. Thumm, G. Gantenbein, R. Heidinger, A. Meier, W. Kasparek, C. Lechte, A. Litvak, G. G. Denisov, A. V. Chirkov, E. Tai, L. G. Popov, V. Nichiporenko, V. E. Myasnikov, E. A. Solyanova, S. A. Malygin, F. Meo, and P. Woskov, Nucl. Fusion, **48**, 054006 (2008).

[26] D. Wagner, G. Grünwald, F. Leuterer, A. Manini, F. Monaco, M. J. Münich, H. Schütz, J. Stober, H. Zohm, T. Franke, M. Thumm, R. Heidinger, G. Gantenbein, A. Meier, W. Kasparek, C. Lechte, A. G. Litvak, G. G. Denisov, A. V. Chirkov, E. M. Tai, L. G. Popov, V. O. Nichiporenko, V. E. Myasnikov, E. A. Solyanova, S. A. Malygin, F. Meo, and P. P. Woskov, IEEE Trans. Plasma Sci., **36**, 324 (2008).

[27] V. Furtula, P. K. Michelsen, F. Leipold, M. Salewski, S. B. Korsholm, F. Meo, S. K. Nielsen, M. Stejner, D. Moseev, and T. Johansen, Rev. Sci. Instrum., **81**, 10D913 (2010).

[28] V. Furtula, P. K. Michelsen, F. Leipold, M. Salewski, S. B. Korsholm, F. Meo, S. K. Nielsen, M. Stejner, D. Moseev, and T. Johansen, Fusion Sci. Tech., **59**, 670 (2011).

[29] T. Geist and M. Bergbauer, Int. J. Infrared Millimeter Waves, **15**, 2043 (1994).

[30] G. G. Denisov, S. Kuzikov, and M. Y. Shmelyov, 18th Int. Conf. on Infrared and Millimeter Waves, **2104**, 353 (1993).

[31] G. G. Denisov, A. A. Bogdashov, A. N. Panin, and Y. V. Rodin, 33rd Int. Conf. on Infrared, Millimeter and Terahertz Waves, 140 (2008).

[32] G. G. Denisov, S. V. Kuzikov, and D. A. Lukonikov, Int. J. Infrared Millimeter Waves, **16**, 1231 (1995).

[33] S. A. Maas, *Nonlinear Microwave and RF Circuits* (Artech House, Inc., Norwood, MA 02062, 2003).

[34] T. H. Lee, *The Design of CMOS Radio-Frequency Integrated Circuits* (Cambridge, University Press, The Pitt Building, Trumpington Street, Cambridge, UK, 2004) pp. 390–400.